Supporting Information for: Trion Formation Hampers Single Quantum Dot Performance in Silane-Coated $FAPbBr_3$ Quantum Dots

Jessica Kline[1], Shaoni Kar[2], Benjamin F. Hammel[3], Yunping Huang[4], Zixu Huang[1], Seth R. Marder[3,4,5], Sadegh Yazdi[3,5], Gordana Dukovic[3,5,6], Bernard Wenger[7], Henry Snaith[2], David S. Ginger[1]*

[1]Department of Chemistry, University of Washington, Seattle, WA 98195, USA

[2] Department of Physics, University of Oxford, Clarendon Laboratory, Parks Road, Oxford, OX1 3PU, UK

[3]Materials Science and Engineering, University of Colorado Boulder, Boulder, CO 80309-0215, USA

[4]Department of Chemical and Biological Engineering, University of Colorado Boulder, Boulder, Colorado 80303, United States

[5]Renewable and Sustainable Energy Institute, University of Colorado Boulder, Boulder, CO 80309-0215, USA

[6]Department of Chemistry, University of Colorado Boulder, Boulder, CO 80309-0215, USA

[7]Helio Display Materials Limited, Wood Centre for Innovation, Quarry Rd, Headington, Oxford OX3 8SB, UK

Table of Contents

Synthesis

Chemicals

Formamidine acetate (99%), oleic acid (OA, ≥ 99%), octadecene (ODE, 90%), oleylamine (OAm, 70%), trioctylphosphine oxide (TOPO, 99%), hexanes (≥ 95%), toluene (anhydrous 99.8%), octane (anhydrous ≥ 99%), formamidinium bromide (FABr, ≥ 98%), isopropanol (IPA, 90%), ethyl acetate (≥ 99%), acetonitrile (≥ 99%), N-(2-aminoethyl)-3-aminopropyltriethoxysilane (AEAPTES) and Ludox TMA (34 wt.%) were purchased from Millipore Sigma. Lead (II) bromide ($PbBr_2$, 99.998% metals basis) was purchased from Alfa Aesar. All chemicals were used as received. $PEAC_8C_{12}$ was synthesized according to Morad et al.[1]

$PEAC_8C_{12}$-passivated $FAPbBr_3$ synthesis

0.08 M $PbBr_2$-TOPO and 0.12 M FA-OA solutions were prepared according to Morad et al.[1] A 0.05 M solution of $PEAC_8C_{12}$ was prepared by dissolving 42 mg (0.10 mol) $PEAC_8C_{12}$ in 2 mLs of a 1:1 mixture of IPA and toluene. 260 µL of the $PbBr_2$-TOPO solution and 100 µL of the FA-OA solution were added to 5 mLs of hexanes and allowed to react while stirring for 30 s. After 30 s, 240 µL of the $PEAC_8C_{12}$ solution were added and the mixture was allowed to react for another 30s. The quantum dots were then washed with a 2:1 mixture of ethyl acetate and acetonitrile and centrifuged at 10 krpm for 5 minutes. The precipitate was dissolved in 2 mLs hexanes and stored in the glovebox.

Silane-coated $FAPbBr_3$ synthesis

Formamidinium lead bromide ($FAPbBr_3$) nanocrystals were synthesized via a conventional hot-injection method. In a typical procedure, 0.2 mmol of $PbBr_2$ was dissolved in 5 mL of octadecene (ODE) containing 0.5 mL of oleic acid (OA) and 0.5 mL of oleylamine (OAm) under nitrogen atmosphere. The mixture was dried under vacuum at 120 °C for 30 min to remove moisture and oxygen and then heated to 170 °C. A precursor solution of formamidinium bromide (FABr, 0.2 mmol) dissolved in 2 mL of ODE was swiftly injected into the hot $PbBr_2$ solution. The reaction mixture was quenched after 7 s by immersion in an ice–water bath, yielding a bright green colloidal dispersion. The crude solution was centrifuged at 6000 rpm for 5 min after the addition of 10 mL of methyl acetate to precipitate the nanocrystals, which were then redispersed in toluene for further processing.

To improve surface passivation and environmental stability, the as-synthesized $FAPbBr_3$ nanocrystals were subjected to post-synthetic ligand exchange using AEAPTES. In a typical treatment, a 0.1 mL aliquot of AEAPTES was added dropwise to 5 mL of the nanocrystal dispersion in toluene (≈5 mg mL^{-1} concentration) under inert conditions. The mixture was stirred for 30 min at room temperature, and the exchanged nanocrystals were purified by adding acetone (3× volume) to induce precipitation, followed by centrifugation and redispersion in toluene. The resulting AEAPTES-capped $FAPbBr_3$ nanocrystals exhibited enhanced colloidal stability and photoluminescence retention under ambient conditions.

Characterization

Ensemble Optical Characterization

Absorbance spectra of the QD solutions were performed using a Perkin-Elmer Lambda 950 UV/Vis/NIR Spectrometer in a range of 400-600 nm with an integration time of 0.5 s. Absorbance spectra were transformed from wavelength to their Einstein B spectrum according to Equation S1.[2]

$$A(E) \propto {}^{A(\lambda)}/_{\nu} \quad \text{(S1)}$$

Steady-state photoluminescence spectra were acquired *via* a home-built fluorescence set up. Dilute solutions (OD of 0.0001 at 405 nm) were excited with a 405 nm laser (CrystaLaser) and spectra

were collected on an OceanHDX (Ocean Insight). Spectral correction was performed using a calibrated white light source (Ocean Insight HL-3P-INT-CAL) to correct for the responsivity of the detector. Photoluminescence spectra were converted from wavelength to energy and corrected for line shape analysis according to Equation S2.[2]

$$I(E) \propto {}^{I(\lambda)}/_{\nu^3 E^2} \tag{S2}$$

Photoluminescence quantum yield measurements (PLQY) were performed on a commercial integrating sphere system (Hamamatsu Photonics K.K). PLQY values are determined using a white light source (Hamamatsu Mercury Xenon Lamp) and a monochromator for wavelength selection (405 nm) as the excitation source to illuminate the samples in an integrating sphere (Hamamatsu Photonics K.K). The optical density of samples was kept below 0.1 at the excitation wavelength to minimize reabsorption effects. Spectral correction was performed using a calibrated white light source (Ocean Insight HL-3P-INT-CAL) to correct for the responsivity of the detector.

Time resolved photoluminescence measurements at 470 nm excitation were acquired using a commercial PicoQuant FluorTime 100 system with LDH-470 laser diode, a 470 nm picosecond pulsed diode laser. The repetition rate is controlled by an external trigger input from a PicoHarp PDL 800-B laser driver and was set to 1 MHz. A photomultiplier tube (PMT) detector was used in TCSPC mode with an instrumental response function (IRF) of approximately 400 ps. The instrument response function (IRF) was measured via laser scatter from a solution of Ludox. Lifetimes were fit to a stretch exponential (Equation S3) using a custom IRF-reconvolution python package.

$$I(t) = A \exp\left(-\frac{t}{\tau_k}\right)^{\beta} + C \tag{S3}$$

Where A is the pre-exponential factor, τ_k is the lifetime of the decay, C is the background of the measurement and β is the distribution of decay rates. τ_{str}, the average lifetime of a stretch exponential, is calculated according to Equation S4 where Γ is the gamma function.[3]

$$\tau_{str} = \frac{\tau_k}{\beta}\Gamma\left(\frac{1}{\beta}\right) \tag{S4}$$

Single Quantum Dot Optical Characterization - Widefield

Single quantum dot films were prepared by diluting quantum dot stock solutions by a factor of 1,000 in toluene. 60 µL of this dilute solution was then spun coat onto a clean [4] low fluorescence glass coverslips (VistaVision #1.5 22x22 mm, VWR) at 2,000 rpm for 40 seconds.

Widefield microscopy measurements were performed on a Nikon TE2000 inverted optical microscope using a CFI Super Fluor 40x Oil immersion objective (NA = 1.3), with Olympus F immersion oil. The illumination source was a 415 nm LED (SOLIS-415C, Thor Labs) at a power density of 9 mW/cm^2. The following filters were used for the measurement: ET510/80m (Chroma), FF01-424/SP-25 (Semrock) and ZT442rdc (Chroma) mounted in Chroma Laser TIRF for Nikon TE2000/T filter cube. Videos of the sample photoluminescence in time were collected on a Prime 95B (Photometrics) camera for 6 minutes and 40 seconds (8000 total images) with an integration time of 50 ms per image.

Single Quantum Dot Optical Characterization - Confocal

Single quantum dot films were prepared by diluting quantum dot stock solutions by a factor of 1,000 in toluene. 60 µL of this dilute solution was then spun coat onto a clean [4] 1 mm thick quartz microscope slide (SPI) at 2,000 rpm for 40 seconds.

Single quantum dot optical characterization was carried out on a home-built confocal microscope integrated with a cryostat (AttoDry800, Attocube). Samples were illuminated with a pulsed 472 nm laser (15.647 MHz, 95 W/cm^2, NKT Photonics). The laser is cleaned up by a bandpass filter (ET470/24m, Chroma) and focused ($1/e^2$ = 1.7 μm) by an objective inside the cryostat (NA = 0.82) onto the sample, and the same objective collects the emitted light. The collected light is passed through a dichroic (Di02-R488, Semrock), a notch filter (ZET473NF, Chroma) and a bandpass (ET520/20m, Chroma) to filter out residual light from the excitation laser and substrate autofluorescence. The collected light is then sent to either a spectrometer and electron-multiplying charge-coupled device camera (Isoplane 320 and Pixis 400, Princeton Instruments) or a Hanbury Brown-Twiss interferometer. The Hanbury Brown-Twiss interferometer consists of a 50/50 beam splitter, two avalanche photodiodes (35 ps IRF, Micro Photon Devices) and photon counting electronics (Swabian) enabling the acquisition of time-tagged time-resolved (TTTR) data. Single quantum-dot measurements were carried out in the weak excitation regime at a fluence of 6.1 μJ/cm^2.

At room temperature quantum dot spectra were obtained with an integration time of 20 seconds on a 600 lines/mm grating. Substrate autofluorescence was subtracted from the spectra and then the spectra were corrected for detector sensitivity using a calibrated white light source (Ocean Insight HL-3P-INT-CAL). Spectra are converted from wavelength to energy (Equation S2) and fit to a single Gaussian of the form:

$$I(E) = {}^{A}/_{\sigma\sqrt{2\pi}} \exp\left[-0.5\left({}^{(E-\mu)}/_{\sigma}\right)^2\right] + b \qquad \text{(S5)}$$

Where A is the amplitude, b is the background, μ is the center of the peak and σ is the standard deviation of the peak. TTTR data was then acquired on the quantum dots for 600 seconds. TTTR data was analyzed using a modified version of the poissonian noise Change Point Analysis (CPA) package from Palstra et al [5] (see **Data Analysis** for more details).

At 4K quantum dot spectra were obtained with an integration time of 1 second on a 600 lines/mm grating. 300 spectra were acquired sequentially after which 600 seconds of TTTR data was acquired followed by the acquisition of another 300 sequential spectra. For each of the 600 spectra substrate autofluorescence was subtracted from the spectra and then the spectra were corrected for detector sensitivity using a calibrated white light source spectra are converted from wavelength to energy (Equation S2) are fit by a single Gaussian (Equation S5). Spectra with less than 10% of the area of the most intense spectrum are considered OFF and are not factored into the analysis further. The time integrated single quantum dot spectrum is the summation of qualifying single frame spectra.

Scanning Transmission Electron Microscopy (STEM)

STEM was performed with a Thermo Fisher Scientific Titan Themis operated at 300kV. Samples were prepared by drop-casting solutions of $FAPbBr_3$ QDs onto ultrathin carbon film TEM grids (Ted Pella, Prod # 01824, ultrathin carbon film on lacey carbon support film, 400 mesh, Cu). To minimize air exposure, grid prep was performed in a glovebox with an argon atmosphere. After drop-casting, the grids were dried under vacuum in the glovebox antechamber for roughly 30 min, before being transferred back into the glovebox, sealed in an air-tight container, and transported to the microscopy facility.

Size analysis was performed using ImageJ (version 1.54f), specifically the FIJI distribution. Particles were segmented using the Trainable Weka Segmentation plug-in (v3.3.4). The particle areas were measured using the "Analyze Particle" function in ImageJ, with size limits set from 25 – 50 nm2 and shape limits from circularity = 0.5 to 1.0 to exclude noise, secondary, or aggregated particles.

Attenuated Total Reflectance Infrared Spectroscopy (ATR-IR)

ATR-IR was performed in the solid-state on a PerkinElmer Frontier FT-IR spectrometer. Samples were prepared by drop-casting quantum dot solutions on indium tin oxide-coated glass substrates.

Data Analysis

Widefield Blinking Data

The analysis of widefield blinking data is described in detail in Gallagher et al.[4] But in brief we identify individual quantum dots in a video using the Laplacian of Gaussian method and process the blinking data using a version of CPA adapted for a Gaussian-distributed time series as published by Yang et al.[6] . Our particle selection and CPA code is publicly available at: https://github.com/GingerLabUW/Widefield-CPA.

TTTR Data

Single quantum dot lifetimes were fit using a custom IRF-reconvolution python package. At room temperature the lifetimes were fit to a stretch exponential (Equations S3 and S4). At 4K the lifetimes were fit to a biexponential (Equation S6) where τ_{fast} was assumed to capture the lifetime of the bright triplet and τ_{slow} is due to emission from the dark singlet.[7]

$$I(t) = A \exp\left(-\frac{t}{\tau_{fast}}\right) + (1-A)\exp\left(-\frac{t}{\tau_{slow}}\right) + C \quad \text{(S6)}$$

Classification of the TTTR blinking traces was performed using a modified version of the poissonian noise CPA package from Palstra et al[5]. Our code is publicly available at: https://github.com/GingerLabUW/Cryostat-Data-Processing. We chose to apply an additional penalty after the "true" number of states was returned by the Bayesian Information Criterion which limited the fit based on the physical constraints of the system. Since three times standard deviation of the dark noise is 150 cps in our system, we reduce the number of "true" states by one until the splitting between all identified intensity levels is at least 150 cps.

As perovskite QDs exhibit multi-level blinking, we find that the traditional ON, OFF and GREY definitions are insufficient to capture the data. Traditionally the ON state is the CPA identified maximum intensity level, the OFF state is anything below the average dark counts + 3 standard deviations, and any other states are GREY. In our data set these definitions result in traces which are classified as around 70% GREY on average, meaning that most of our data is effectively being thrown out. Instead, we choose to treat our GREY states as representing a linear combination of our traditionally defined ON and OFF states. Which can be rationalized as either due to fast blinking events or an instantaneous k_{nr} which is similar to the k_r as in the ON state $k_r >> k_{nr}$ and in the OFF state $k_{nr} >> k_r$. As such we can calculate the weighted ON and OFF fractions for each trace as shown in Equations S7a-c.

$$I_n = a_n I_{ON} + (1-a_n) I_{OFF} \quad \text{(S7a)}$$

$$f_{ON} = \sum_n a_n T_n \quad \text{(S7b)}$$

$$f_{OFF} = \sum_n (1-a_n) T_n \quad \text{(S7c)}$$

Where I_{ON} is the CPA identified maximum intensity level, I_{OFF} is the average APD dark counts + 3 standard deviations (300 cps at room temperature, 500 cps at 4K), I_n is any CPA identified intensity level, a_n is the fraction of ON character in an intensity level and T_n is the fraction of total measurement time spent in the intensity level. For example, for the quantum dot shown in Figure S6 our methodology classifies the blinking trace as 37% ON and 63% OFF which we find is a better descriptor than traditional ON/OFF/GREY classification (26% ON, 47% OFF and 27% GREY) or traditional ON/OFF classification (53% ON and 47% OFF).

To fit fluorescence lifetime intensity distributions (FLIDs) we find the lifetime of each CPA identified intensity level. We consider two primary non-radiative decay mechanisms which can be responsible for blinking in these quantum dots.[8] Non-radiative band-carrier (BC) recombination which can occur in a neutral quantum dot and non-radiative Auger recombination which can occur in a photoionized quantum dot. The expected lifetime intensity relationships are described in Equations S8a and b respectively. As individual quantum dots can experience both BC and Auger blinking during a measurement the measured lifetime intensity correlation is fit to a linear combination of BC and Auger blinking (Equation S8c). Single QD FLIDs were not lifetime or intensity normalized before fitting to Equation S8. FLIDs were only normalized to construct the representative average FLIDs shown in Figure 4 in the Main Text. During the normalization process, the lifetime- and intensity- axes were divided by the maximum observed lifetime and intensity respectively.

$$I(\tau)_{Auger} = \frac{I_{ON} I_{OFF,Aug}(\tau_{OFF,Aug} - \tau_{ON})}{I_{OFF,Aug}(\tau_{OFF,Aug} - \tau) + I_{ON}(-\tau_{ON} + \tau)} \quad \text{(S8a)}$$

$$I(\tau)_{BC} = \frac{I_{OFF,BC} - I_{ON}}{\tau_{OFF,BC} - \tau_{ON}} \tau \quad \text{(S8b)}$$

$$I(\tau) = \alpha I(\tau)_{BC} + (1 - \alpha) I(\tau)_{Auger} \quad \text{(S8c)}$$

We use a mono-exponential function to fit the $g^{(2)}(\tau)$ data and determine $g^{(2)}(0)$ (Equations S9a-b).

$$g^{(2)}(\tau) = b + \sum_n A_n \exp\left(^{-|\tau - r_n|}/_{\tau_{TRPL}}\right) \quad \text{(S9a)}$$

$$g^{(2)}(0) = {}^{6 * A_4}/_{(A_1 + A_2 + A_3 + A_5 + A_6 + A_7)} \quad \text{(S9b)}$$

Where b is the constant background counts, A_n is the amplitude of the n-th peak, r_n is the peak of the n-th peak (approximately -192, -128, -64, 0, 64, 127 and 192 ns respectively) and τ_{TRPL} is the average lifetime. $g^{(2)}(0)$ is then determined as the ratio between the area of the peak at zero time delay at the averaged area of the side peaks.

Photoluminescence Components

To look at the components of single quantum dot photoluminescence we first correct the short (1s) integration time spectra for spectral variations in time (blue shifting and spectral diffusion) according to Gumbsheimer et al.[9] The 600 short time spectra were then summed into one long time (600 s) spectrum.

To fit single quantum dot photoluminescence components, we consider five contributors – the zero phonon line (ZPL) at 0 meV, optical phonon 1 (OP_1) at -4.9 meV, optical phonon mode 2 (OP_2) at -19.5 meV, trion emission (X*) and biexciton emission (XX). Each component is considered to have a gaussian contribution with equal standard deviations and different emission maxima/heights as described in Equation S10.

$$I(E) = g(a, 0, \sigma)_{zpl} + g(a, -4.9, \sigma)_{op1} + g(a, -19.5, \sigma)_{op2} + g(a, \mu, \sigma)_{x*} + g(a, \mu, \sigma)_{XX} + b \quad \text{(S10)}$$

The emission maxima of the ZPL, OP_1 and OP_2 contributions are fixed to 0, -4.9 and 19.5 meV respectively[10–12] and the emission maxima of the X* and XX contributions are fit. Based on the reported trion and biexciton binding energies in the literature we constrain the emission maxima of the trion between -40 and -20 meV and the biexciton between -60 and -30 meV.[10] The standard deviation of the Gaussians is constrained between 5 and 15 meV. Additionally we constrain the intensity of the optical phonon emission peaks based on the reported strength of these peaks in ~ 6 nm $FAPbBr_3$ quantum dots. OP_1 must be between [0.5, 1]*a_{zpl}, and OP_2 is constrained between [0.01, 0.15]*a_{zpl}.[11,12]

Fluence Dependent PLQY

We estimate the PLQY of the quantum dot thin films by first measuring the PLQY of the quantum dot thin films at room temperature in an integrating sphere. We then measure the intensity of our films on the confocal-integrated cryostat at room temperature using our lowest excitation power (4.5E-4 μJ/cm^2). The film intensities were determined by averaging the intensity of six 29x29 μm scans acquired with a resolution of 0.5 μm. The films were subsequently cooled down to 4K and another series of six 29x29 μm scans were acquired with a resolution of 0.5 μm to determine the average film intensity at 4K. The dwell time at each pixel was less than 50 ms to prevent photobleaching from affecting the measurement. We assume that the absorbance cross section does not change between room temperature and 4K and as such the PLQY at 4K equal to the room temperature PLQY scaled by the change in film intensity.

The absorption cross section of the films were determined by fitting the long-time photoluminescence intensity to:

$$I = q * (1 - e^{-\sigma j}) \tag{S11}$$

Where q is the quantum yield at a given fluence, σ is the absorption cross section and j is the incident fluence in photons/cm^2.

During the fitting process we constrain the parameters of Equation 1 in the Main Text as follows. $k_{r,X}$ and $k_{nr,X}$ are fixed by measuring the lifetime and quantum yield of the quantum dots at the lowest fluence, where recombination is dominated by the exciton. Selected fluence dependent lifetimes are shown in Figure S15. The radiative rates of the trion and biexciton are constrained by the expected statistical scaling of radiative rates such that $k_{r,X\pm} = [1.5, 2.5]*k_{r,X}$ and $k_{r,XX} = [3.5, 4.5]*k_{r,XX}$.[13] The non-radiative rate of the trion and trapping rate of the biexciton are free parameters, and the non-radiative rate of the biexciton is constrained by the expected statistical scaling of Auger rates such that $k_{nr,XX} = [3.5, 4.5]*k_{nr,X\pm}$.[13]

Before selecting the model depicted in Figure 5a of the Main Text, we considered many potential models to explain fluence dependent quantum yield changes in quantum dots. These potential models and their fits for our fluence dependent quantum yield data are shown in Figure S16. The three models we primarily considered are: (1) QY roll off due to biexciton formation with no trion formation (2) conversion of the exciton to a dark charged state and a subsequent absorption event to generate a trion and (3) a combination of the dark charged and biexciton pathways for trion formation. QY roll off due to biexciton formation with no trion formation (model 1) is discarded because this model can not capture the experimental QY roll-off of silane-coated quantum dots. Even without constraining the biexciton radiative and non-radiative rates, Model 1 always predicts shallower QY roll-off than experimentally observed in the silane-coated quantum dots. Conversion of the exciton to a dark charged state which can then generate a trion (model 2) is discarded because this model predicts a large steady state population (> 80%) of the dark charged state which is inconsistent with the high weighted ON%s observed in both quantum dot samples. A combination of the dark charged and biexciton pathways for trion formation (model 3) is discarded because of the predicated large steady state population of the dark charged state which is inconsistent with the high weighted ON%s observed in both quantum dot samples and trion and biexciton rate constants which do not converge to a unique solution within reasonable physical bounds.

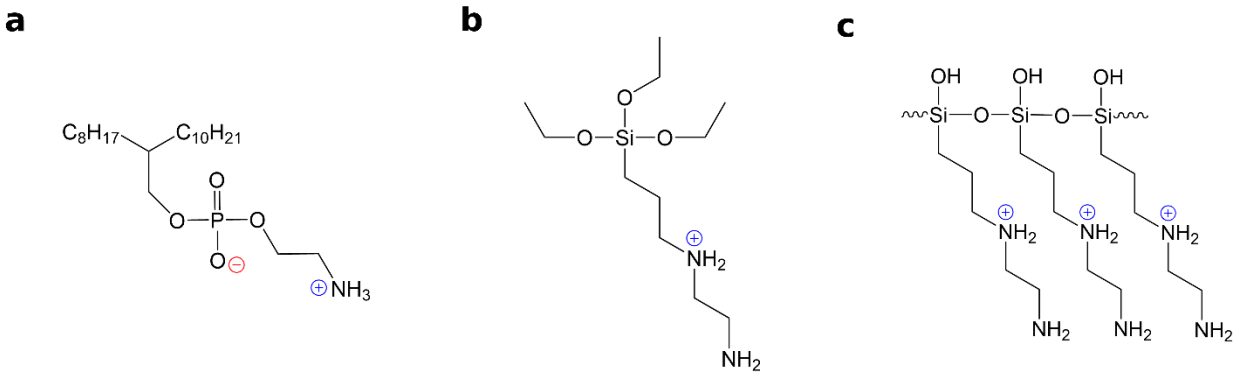

Figure S1. Chemical structures of **a)** $PEAC_8C_{12}$ **b)** mono-protonated N-(2-aminoethyl)-3-aminopropyltriethoxysilane (AEAPTES) and **c)** hydrolyzed mono-protonated AEAPTES. Although AEAPTES is neutral, the acid-base chemistry of our solutions suggests that the functional form of AEAPTES is mono-protonated. Protonation likely occurs via proton transfer from free oleylammonium in solution ($K_{tranfser} \sim 0.3$) and the counterion for mono-protonated AEAPTES takes the form of free oleate or Br-.

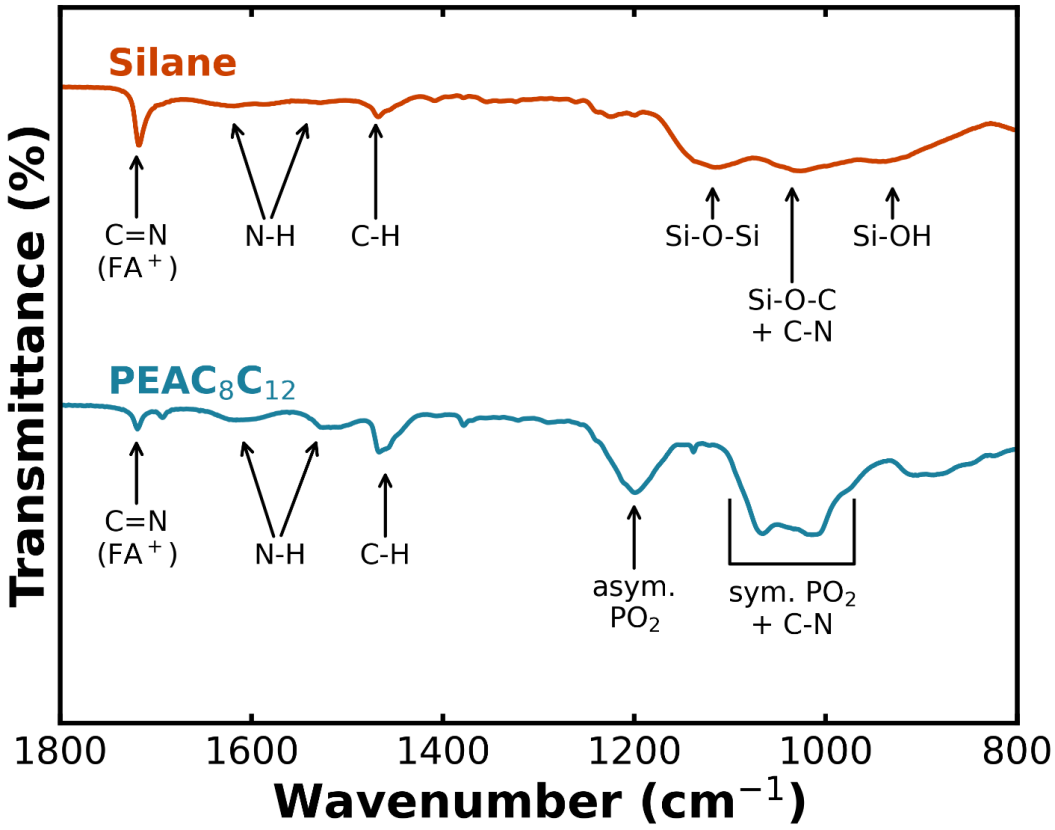

Figure S2. AT-IR characterization of $PEAC_8C_{12}$-passivated (blue) and silane-coated (orange) quantum dot samples. Both samples show C=N stretching from FA^+ and NH and CH bending from the ligands.[1,14,15] $PEAC_8C_{12}$-passivated quantum dots also show PO_2 and C-N stretches.[1] In contrast silane-coated quantum dots show Si-O-Si, Si-O-C, Si-OH and C-N vibrations[1,15] indicating the partial hydrolysis and cross-linking of the triethoxysilane tail.

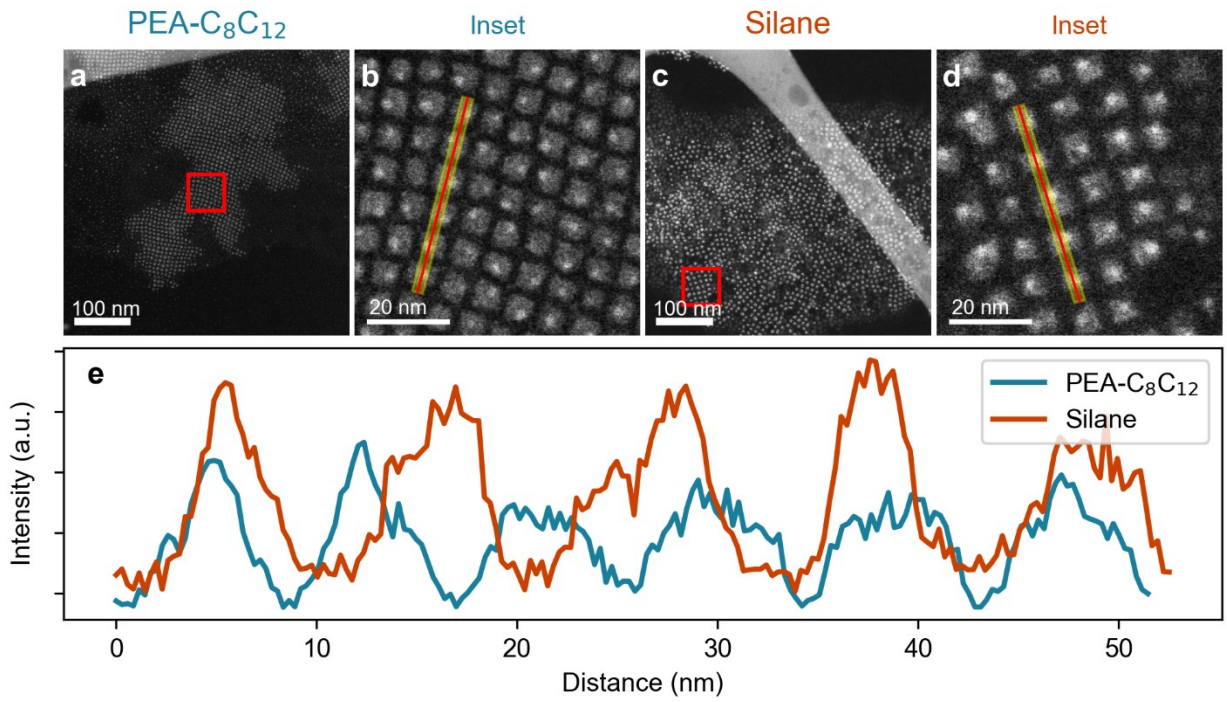

Figure S3. HAADF-STEM images of **a)** $PEAC_8C_{12}$-passivated and **c)** silane-coated $FAPbBr_3$ quantum dots, with insets **b and d)** indicated by the red box in the full image. The red line with yellow highlight illustrates the path and linewidth, respectively, of the line profiles. **e)** Line profiles of HAADF intensity for the $PEAC_8C_{12}$-passivated and silane-coated $FAPbBr_3$ quantum dots. The regular size and shape of the quantum dots encourages the formation of well-ordered regions; line profiles across these regions reveal that the silane-coated quantum dots are slightly larger and have greater distances between particles than the $PEAC_8C_{12}$-passivated quantum dots. This suggests that the silane-coating contributes to the size of the particles as well as the size of the ligand sphere.

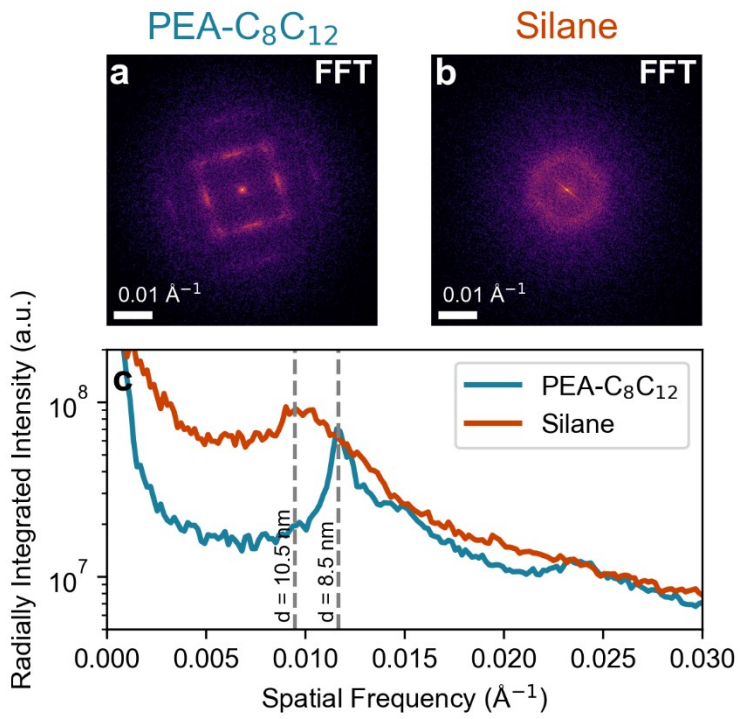

Figure S4. FFTs of HAADF-STEM images of **a)** $PEAC_8C_{12}$-passivated (Figure S2a) and **b)** silane-coated $FAPbBr_3$ quantum dots (Figure S2c). **c)** Radially integrated intensity of the FFTs. To determine the averaging packing distances over the entirety of both HAADF-STEM images, we computed the fast Fourier transformation (FFT). In this case, peaks in the FFT correspond to periodicity in the particle packing. In the image of the $PEAC_8C_{12}$-passivated quantum dots (Figure S2a), the particles are ordered in a large superlattice domains with small orientational mismatches, which results in well-defined peaks. In the image of the silane-coated quantum dots (Figure S2c), there are smaller superlattice domains with different orientations, which results in a less-defined circular pattern. The radial integration of the FFT (Figure S3c) demonstrates that the silane-coated quantum dots are, on average, further spaced than the $PEAC_8C_{12}$-passivated quantum dots. Assuming that the spacing equals the particle size (e.g., the edge length) plus twice the thickness of the ligand sphere, (accounting for the two layers of ligands in the gap between two particles), comparing the spacing (8.5 and 10.5 nm) to the average sizes in Figure 1d (6.2 and 7.3 nm) allows us to estimate ligand sphere thicknesses of 1 nm and 1.5 nm for the $PEAC_8C_{12}$-passivated and silane-coated quantum dots, respectively. Altogether, this suggests that the silane-coating contributes about 0.5 nm to the size of the particles as well as 0.5 nm to the size of the ligand sphere.

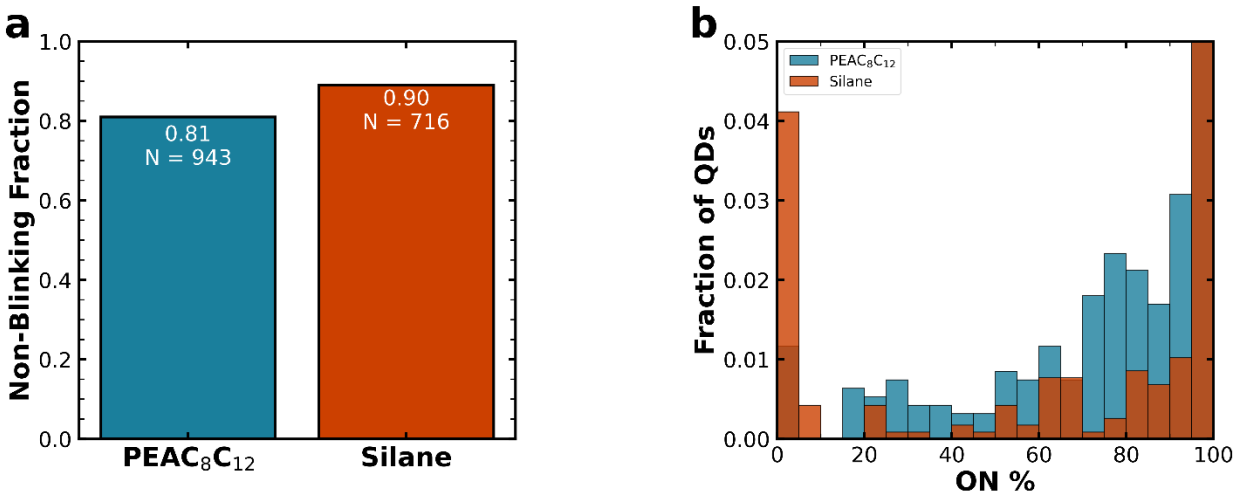

Figure S5. Widefield blinking characterization of single $FAPbBr_3$ quantum dots a) the non-blinking fraction (≥ 95% ON) for both passivation methods **b)** distribution on quantum dot ON% for both passivation methods. In widefield, blinking $PEAC_8C_{12}$-passivated quantum dots tend to blink less than their silane-coated counterparts.

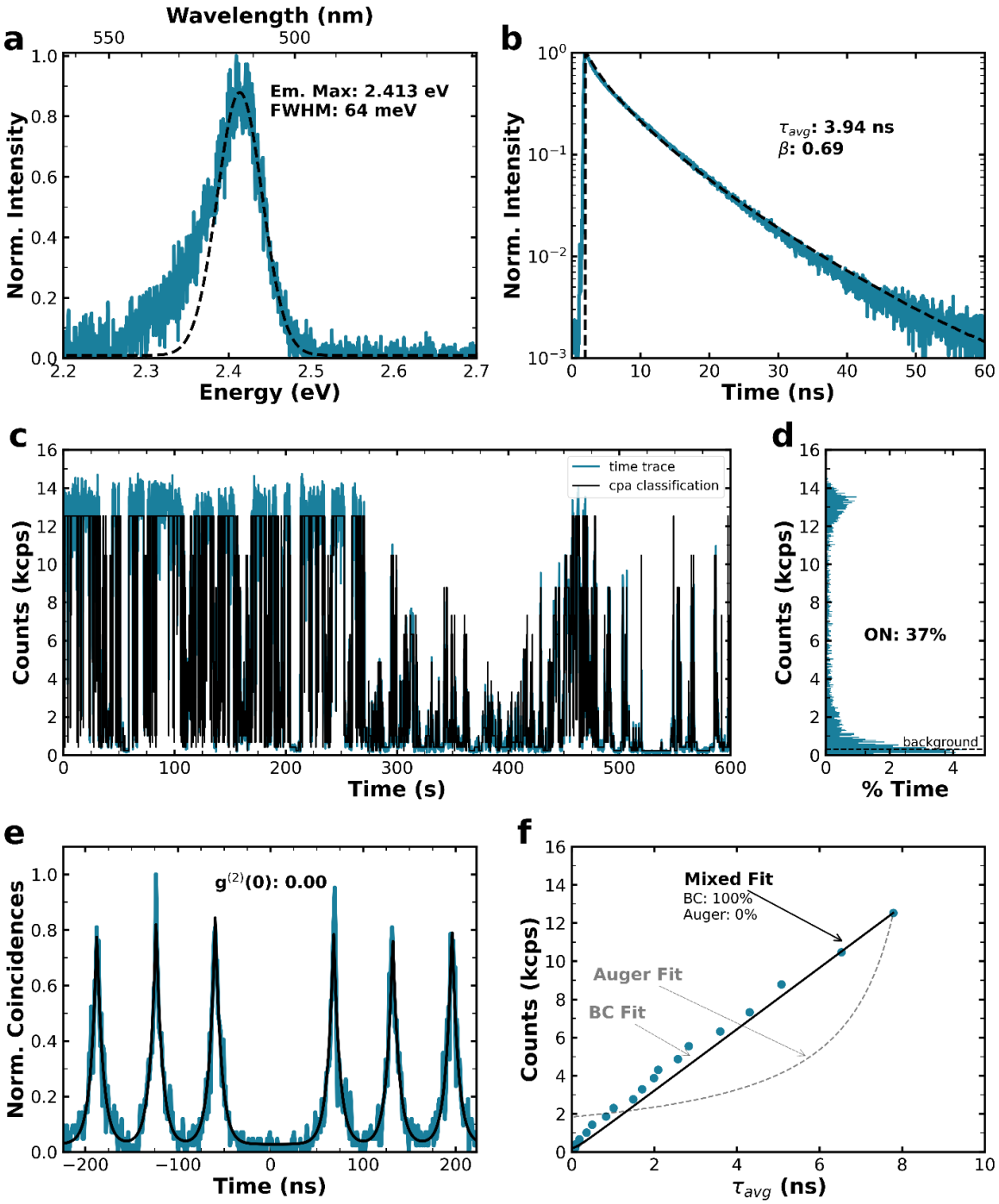

Figure S6. Example room temperature characterization of a single $PEAC_8C_{12}$-passivated $FAPbBr_3$ quantum dot a) the single quantum dot photoluminescence spectrum is shown in blue while the black dashed lines represent the Gaussian fit from which the emission maximum and FWHM are extracted **b)** photoluminescence lifetime (blue) and stretched exponential fit (black dashed line) **c)** experimental blinking trace (blue) and CPA classified blinking trace (black) **d)** photoluminescence intensity histogram **e)** experimental $g^{(2)}(\tau)$ trace (blue) and fit (black) **f)** CPA identified intensity levels correlated to their measure lifetime (blue points). Dashed lines represent the Auger- and BC-type blinking fits (Equations S8a and b) of the data while the solid black line represents the combination of both blinking types.

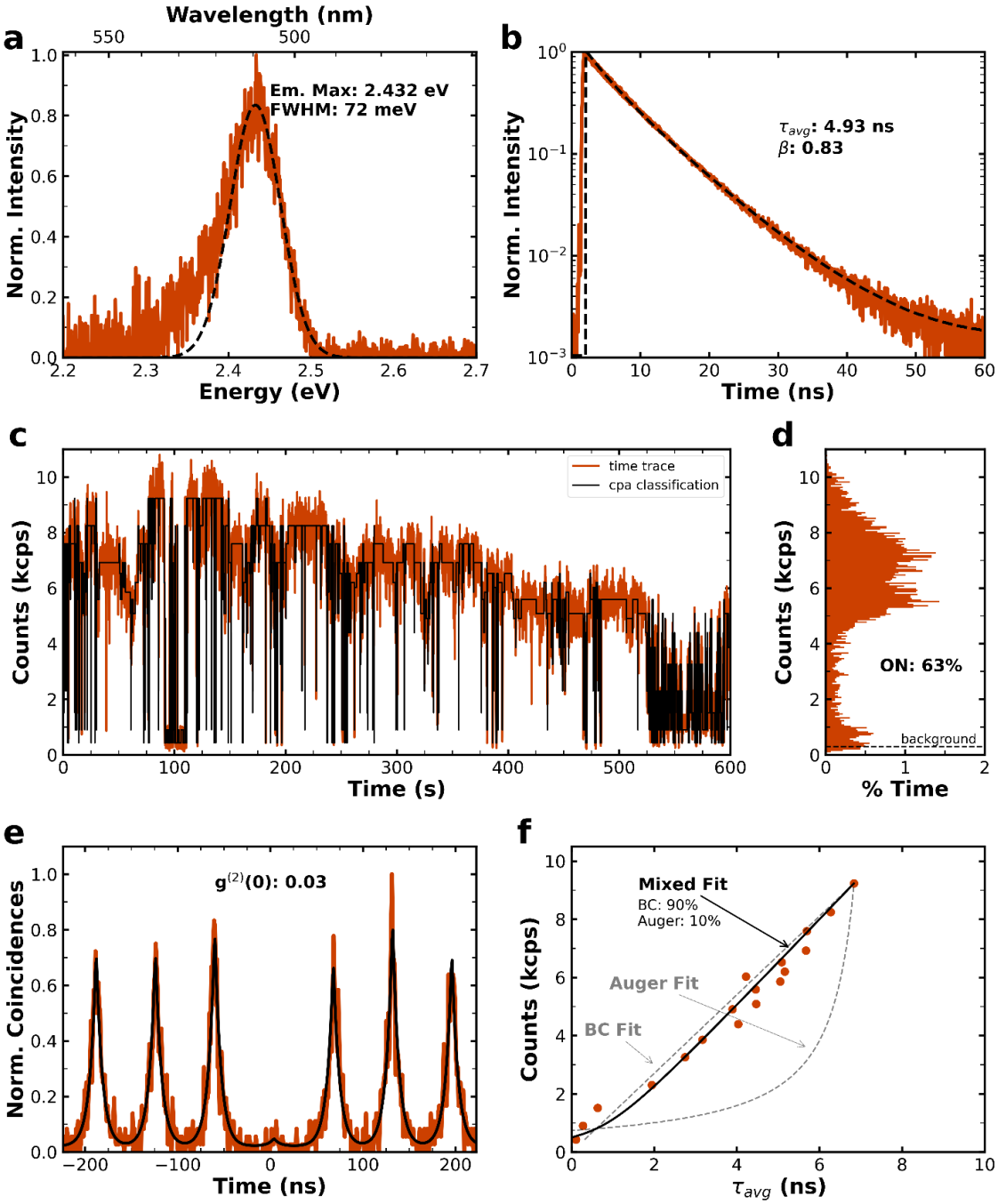

Figure S7. Example room temperature characterization of a single silane-coated $FAPbBr_3$ quantum dot a) the single quantum dot photoluminescence spectrum is shown in orange while the black dashed lines represent the Gaussian fit from which the emission maximum and FWHM are extracted **b)** photoluminescence lifetime (orange) and stretched exponential fit (black dashed line) **c)** experimental blinking trace (orange) and CPA classified blinking trace (black) **d)** photoluminescence intensity histogram **e)** experimental $g^{(2)}(\tau)$ trace (orange) and fit (black) **f)** CPA identified intensity levels correlated to their measure lifetime (orange points). Dashed lines represent the Auger- and BC-type blinking fits (Equations S8a and b) of the data while the solid black line represents the combination of both blinking types.

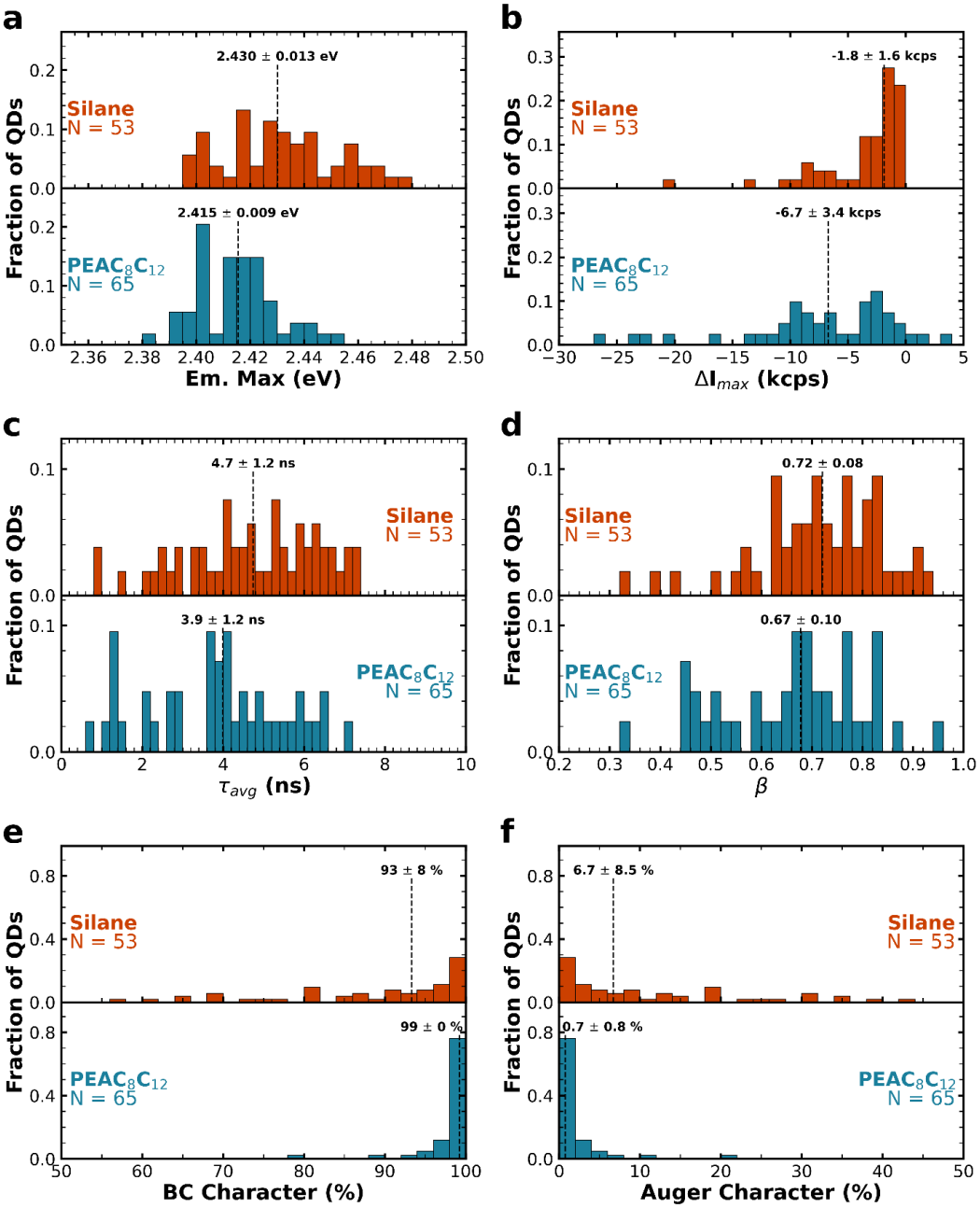

Figure S8. Additional room temperature characterization of single quantum dots a) Distribution of emission maxima. Silane-coated quantum dots have a slightly broader distribution consistent with the broader size distribution seen in TEM. **b)** Distribution of change in maximum intensity over 600 seconds. On average $PEAC_8C_{12}$-passivated quantum dots lose five times more intensity than silane-coated quantum dots. **c)** Distribution of single quantum dot average lifetimes. On average silane-coated quantum dots have a slightly longer lifetime. **d)** Distribution of single quantum dot lifetime homogeneity (beta) factors. On average silane-coated quantum dots tend to have slightly more homogenous lifetimes. Distributions of **e)** BC and **f)** Auger character determined from FLID fitting. Silane-coated quantum dots tend to have more Auger mediated blinking in comparison to $PEAC_8C_{12}$-passivated quantum dots.

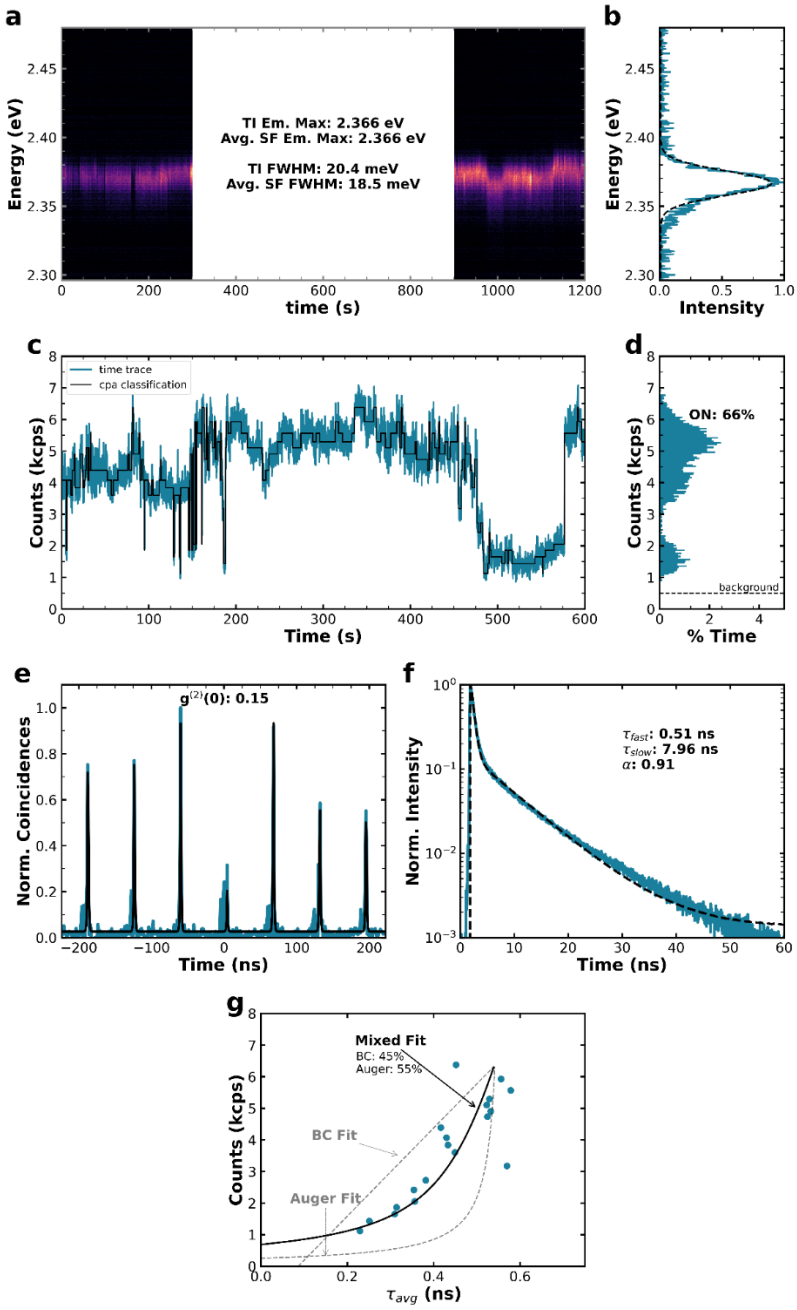

Figure S9. Example 4K characterization of a single $PEAC_8C_{12}$-passivated $FAPbBr_3$ quantum dot a) spectral diffusion trace consisting of 600 spectra with a 1s integration time acquired in two batches of 300 with a 600 s period of TTTR data acquisition in between. The average single frame (SF) spectrum has a peak emission energy of 2.366 eV and a FWHM of 18.5 meV **b)** the time integrated (TI) spectrum of the quantum dot which is the sum of the qualifying SF spectra. The TI spectrum has a peak emission energy of 2.366 eV and a FWHM of 20.4 meV **c)** experimental blinking trace (blue) and CPA classified blinking trace (black) **d)** photoluminescence intensity histogram **e)** experimental $g^{(2)}(\tau)$ trace (blue), and fit (black) **f)** photoluminescence lifetime (blue) and biexponential fit (black dashed line) **g)** CPA identified intensity levels correlated to their measure lifetime (blue points). Dashed lines represent the Auger- and BC-type blinking fits (Equations S8a and b) of the data while the solid black line represents the combination of both blinking types.

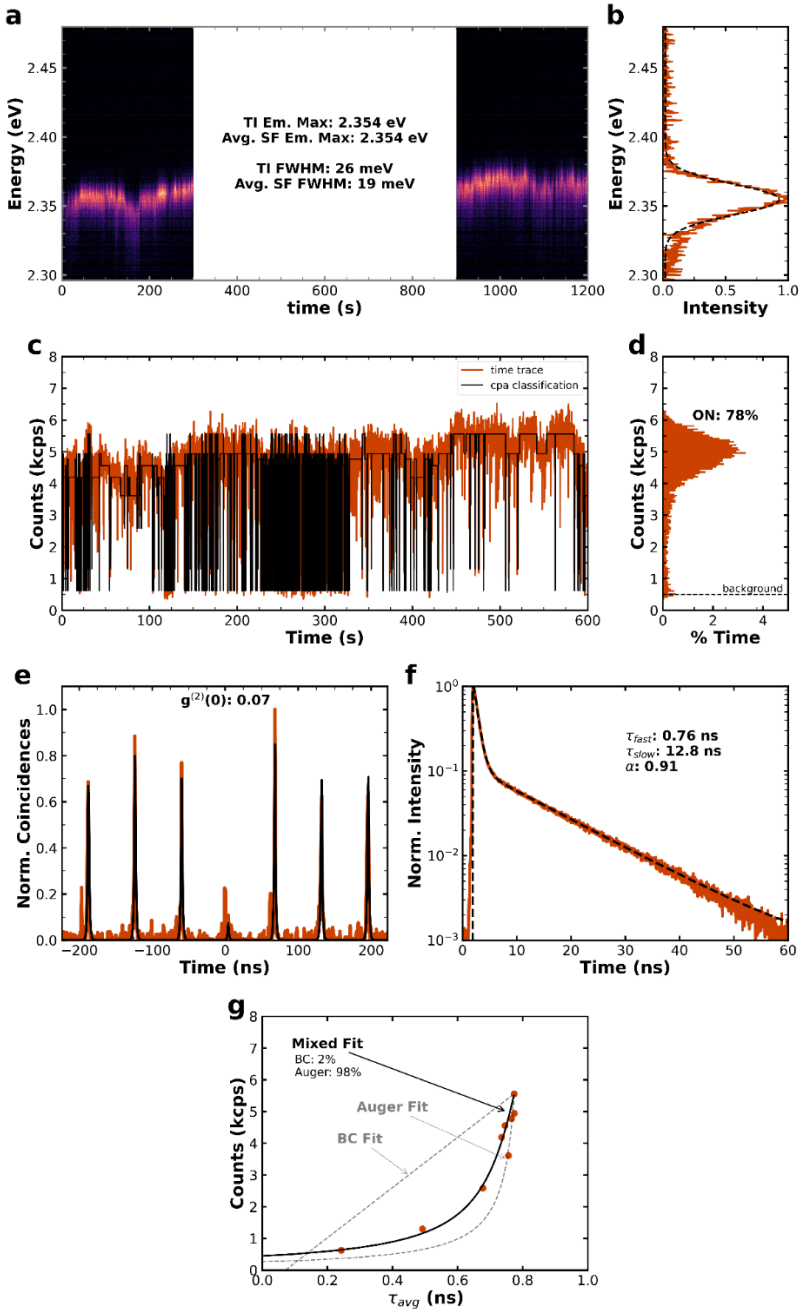

Figure S10. Example 4K characterization of a single silane-coated $FAPbBr_3$ quantum dot a) spectral diffusion trace consisting of 600 spectra with a 1s integration time acquired in two batches of 300 with a 600 s period of TTTR data acquisition in between. The average single frame (SF) spectrum has a peak emission energy of 2.354 eV and a FWHM of 19 meV **b)** the time integrated (TI) spectrum of the quantum dot which is the sum of the qualifying SF spectra. The TI spectrum has a peak emission energy of 2.354 eV and a FWHM of 26 meV **c)** experimental blinking trace (orange) and CPA classified blinking trace (black) **d)** photoluminescence intensity histogram **e)** experimental $g^{(2)}(\tau)$ trace (orange), and fit (black) **f)** photoluminescence lifetime (orange) and biexponential fit (black dashed line) **g)** CPA identified intensity levels correlated to their measure lifetime (orange points). Dashed lines represent the Auger- and BC-type blinking fits (Equations S8a and b) of the data while the solid black line represents the combination of both blinking types.

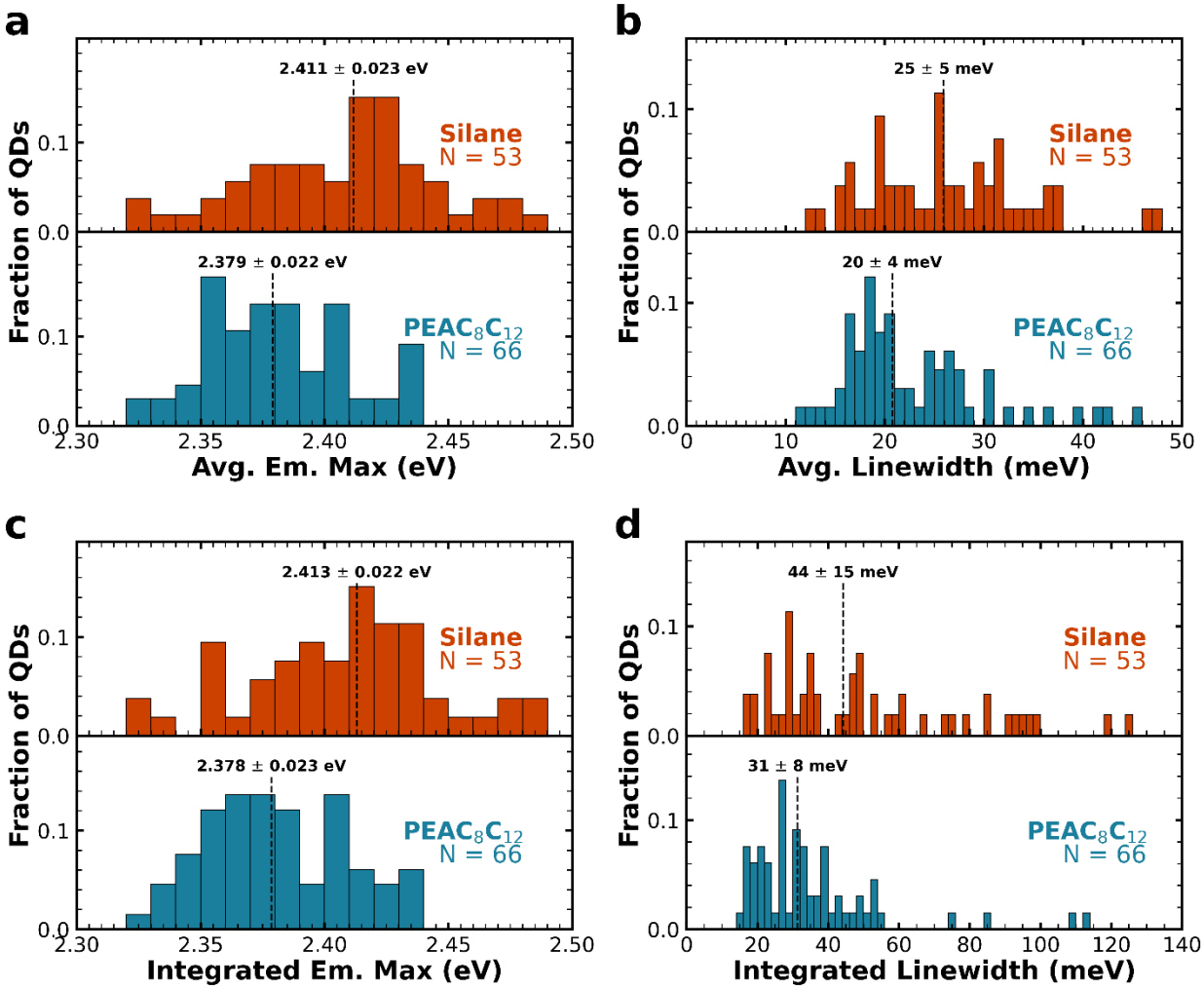

Figure S11. Additional 4K photoluminescence characterization a) Distribution of average single quantum dot emission maximum at short (1s) integration times **b)** Distribution of average single quantum dot linewidths at short (1s) integration times **c)** Distribution of single quantum dot emission maximum at long (600 s) integration times **d)** Distribution single quantum dot linewidths at long (600 s) integration times

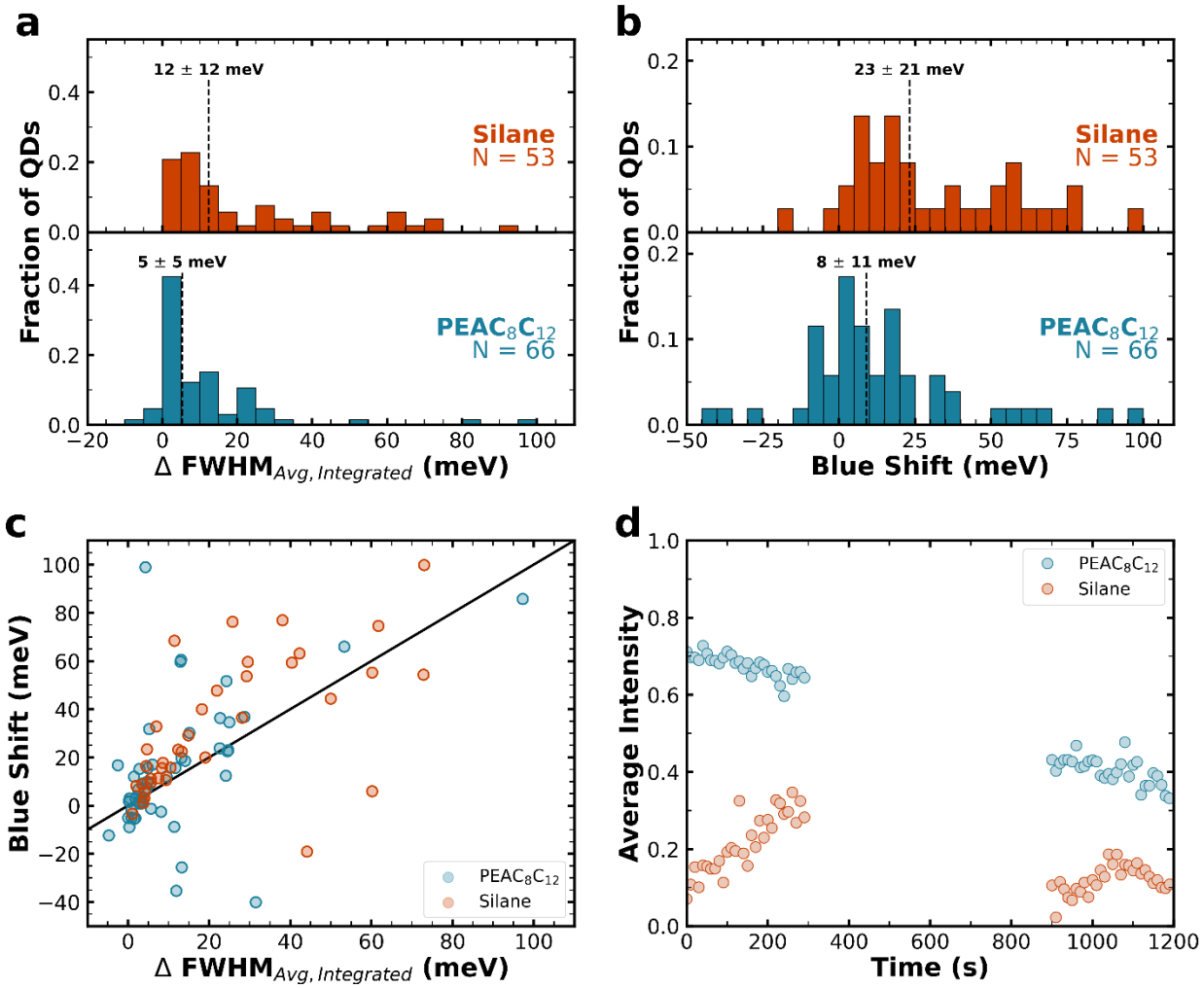

Figure S12. Evidence for Photodegradation at 4K a) Distribution of the change in FWHM between short (1s) and long (600s) integration times. Silane-coated quantum dots FWHMs have broadened twice as much as $PEAC_8C_{12}$-passivated quantum dots. **b)** Distribution of the change in the short integration time emission maximum over twenty minutes of illumination. On average, silane-coated quantum dots have blue shifted three times more than $PEAC_8C_{12}$-passivated quantum dots. **c)** Correlation between changing linewidth and a blue shifting emission maximum. In both samples the broadening of the linewidth with long integration times is strongly correlated with blue shifting emission. **d)** Average intensity of single quantum dot emission in time extracted from photoluminescence spectra. On average, $PEAC_8C_{12}$-passivated quantum dots have higher intensities and less variation in time. Silane-coated quantum dots see both photobrightening and photobleaching during the measurement time and have much larger variations in emission intensity.

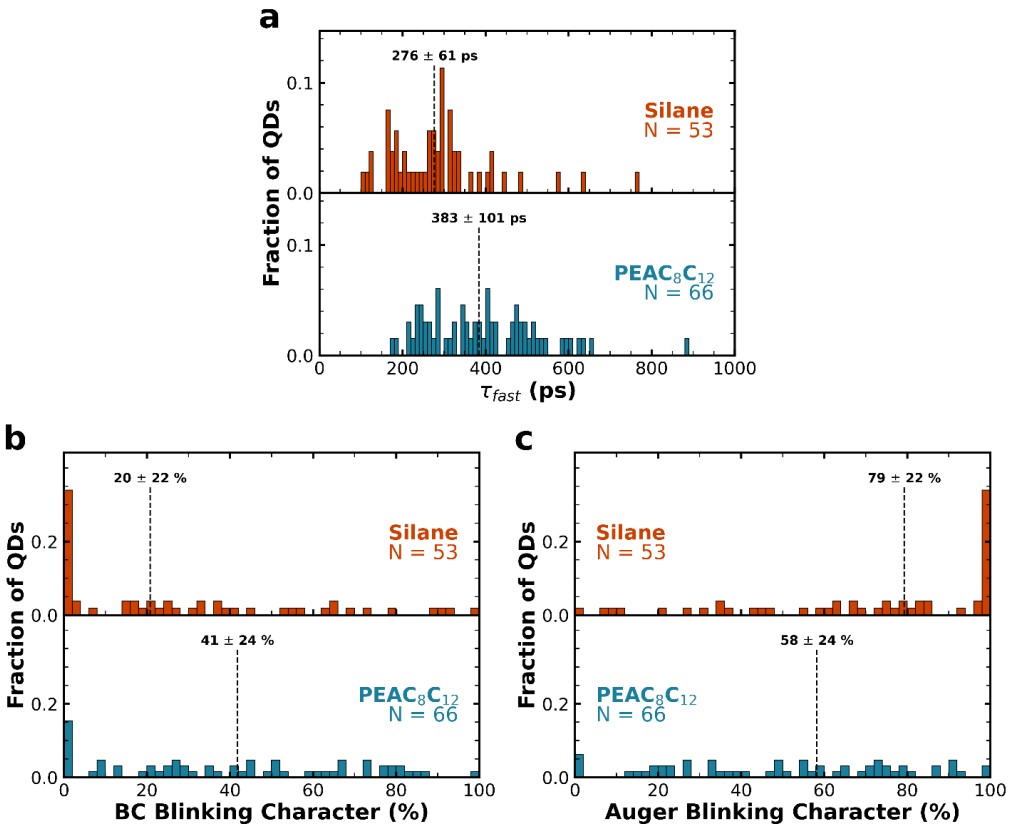

Figure S13. Additional 4K blinking characterization **a)** Distribution over average lifetimes for single quantum dots over ten minutes. On average $PEAC_8C_{12}$-passivated quantum dots have lifetimes 100 ps longer than silane-coated quantum dots indicating better surface passivation by $PEAC_8C_{12}$ at 4K. Distributions of **b)** BC and **c)** Auger character determined from FLID fitting. Silane-coated quantum dots tend to have more Auger mediated blinking in comparison to $PEAC_8C_{12}$-passivated quantum dots.

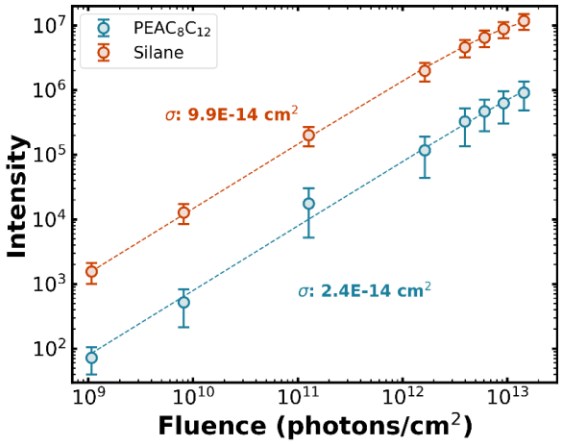

Figure S14. Absorption cross sections determined by fitting the fluence dependent intensity to Equation S11. Silane-coated quantum dots have an absorption cross section of 9.9E-14 cm^2 and $PEAC_8C_{12}$-passivated quantum dots have an absorption cross section of 2.4E-14 cm^2.

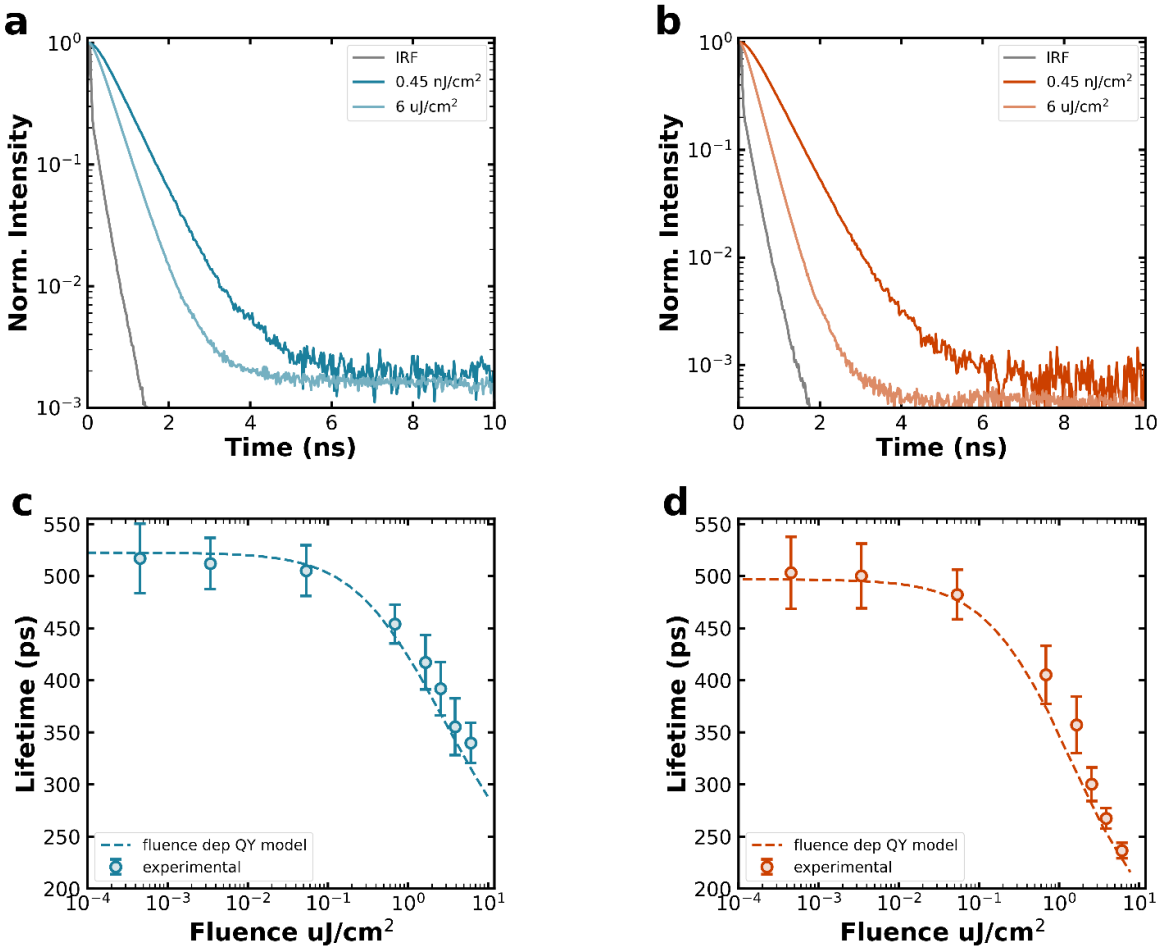

Figure S15. 4K fluence dependent lifetimes. Selected lifetimes for **a)** $PEAC_8C_{12}$-passivated and **b)** silane-coated quantum dots at minimum (0.45 nJ/cm^2) and maximum (6 uJ/cm^2) excitation densities. $k_{r,X}$ and $k_{nr,X}$ of the fluence dependent quantum yield model are extracted from the lifetimes acquired at 0.45 nJ/cm^2. Experimental fluence dependent lifetime for **c)** $PEAC_8C_{12}$-passivated and **d)** silane-coated quantum dots compared to the lifetime predicted from the fit fluence dependent quantum yield.

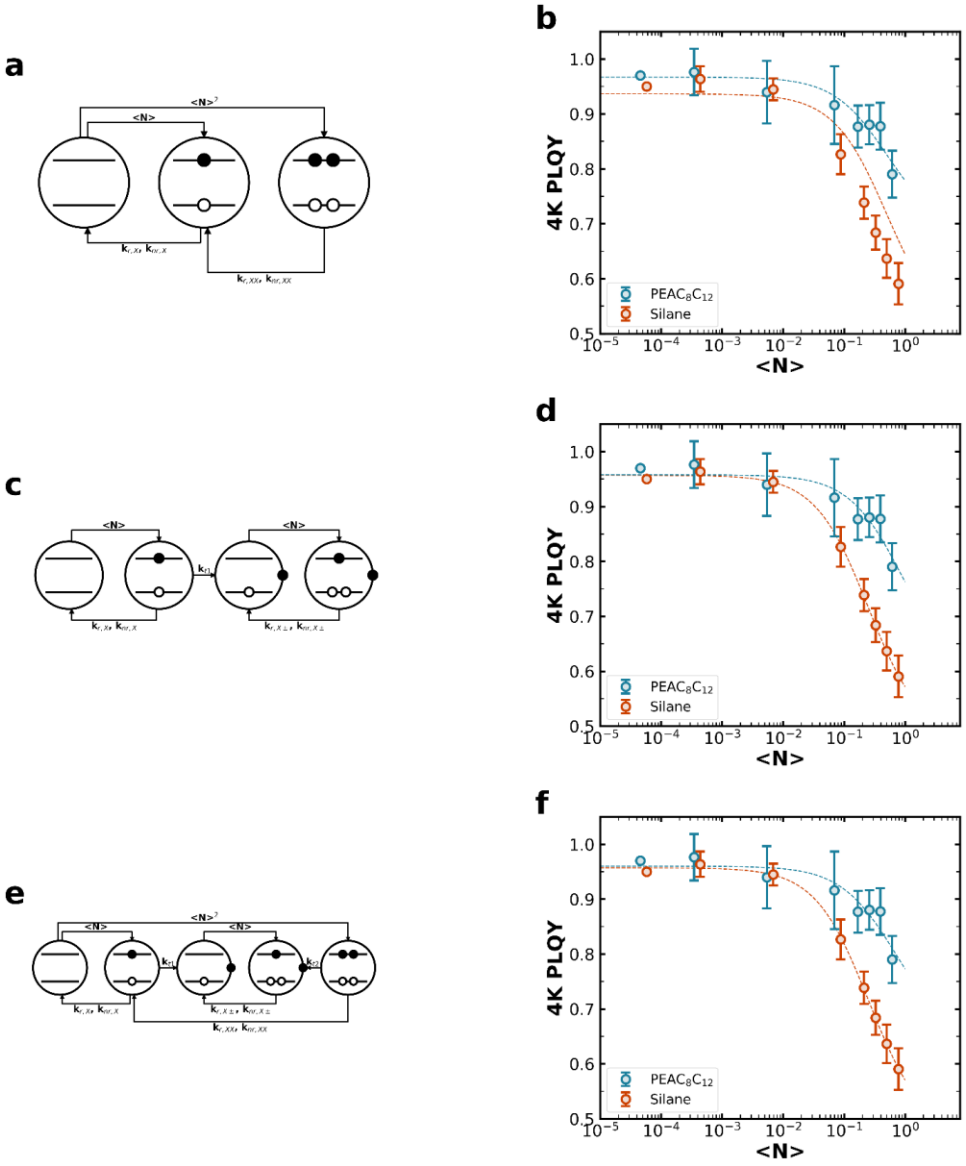

Figure S16. Models for fluence dependent quantum yield in quantum dots a) model for quantum yield changing only based on biexciton formation **b)** fit of biexciton only model to experimental data. This model fails to capture the experimental quantum yield dynamics for silane-coated quantum dots and even with unconstrained biexciton recombination rates the fit roll off is always too shallow. **c)** model for quantum yield changing based on the formation of a dark charged state which can generate trions after a second absorption. **d)** fit of dark charged only model to experimental data. While this model captures the experimental quantum yield dynamics, it predicts a large steady-state population (> 80%) of the dark charged state which is inconsistent with the single quantum characterization of these materials. **e)** model for quantum yield changing based on the formation of a dark charged state which can generate trions after a second absorption and a biexciton which can convert to a trion. **f)** fit of mixed model to experimental data. While this model captures the experimental quantum yield dynamics, it predicts a large steady-state population (> 80%) of the dark charged state which is inconsistent with the single quantum characterization of these materials. Additionally, there is no unique solution for the trion and biexciton rate constants with this fit.

Table S1. Comparison of exciton and biexciton state parameters extracted from fluence dependent PLQY fit (QY) and single quantum dot blinking traces (TRPL)

		Exciton		Biexciton	
		QY	***τ (ps)***	***QY***	***τ (ps)***
$PEAC_8C_{12}$	***QY***	0.96	523 ± 62	0.68	144 ± 27
	TRPL	1	534 ± 140	0.73 ± 0.19	196 ± 51
Silane	***QY***	0.95	500 ± 45	0.39	103 ± 13
	TRPL	1	525 ± 120	0.60 ± 0.13	157 ± 34

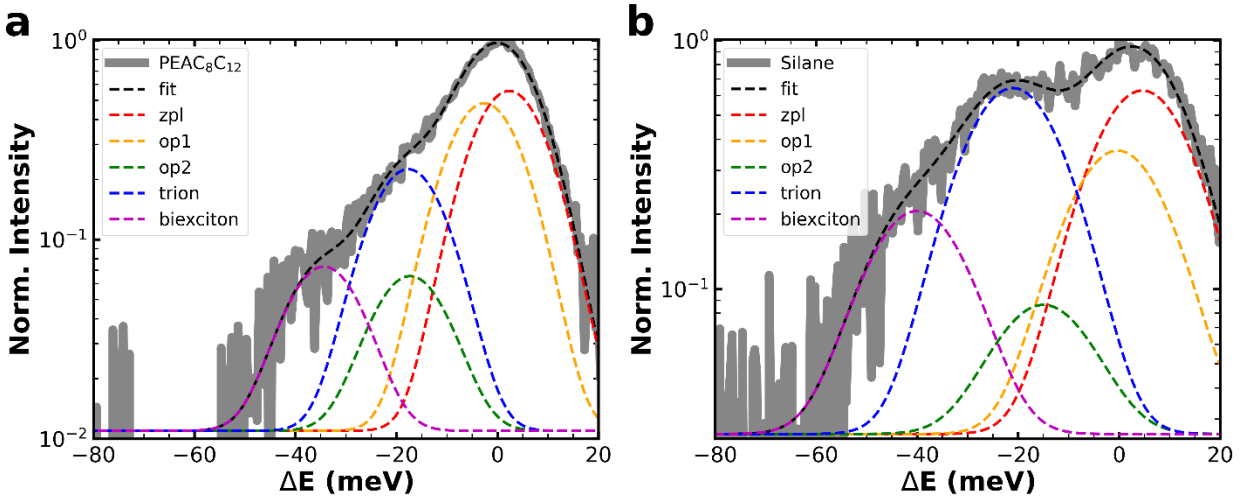

Figure S17. Components of single quantum dot 4K photoluminescence spectra for **a)** $PEAC_8C_{12}$-passivated quantum dots. ZPL (A = 9.2, μ = 0 meV, σ = 6.7 meV), OP1 (A = 7.9, μ = -4.9 meV, σ = 6.7 meV) , OP2 (A = 0.9, μ = -19.6 meV, σ = 6.7 meV) , trion (A = 3.6, μ = -20 meV, σ = 6.7 meV) , biexciton (A = 1.0, μ = -36 meV, σ = 6.7 meV) **b)** silane-coated quantum dots. ZPL (A = 13.2, μ = 0 meV, σ = 8.8 meV), OP1 (A = 7.4, μ = -4.9 meV, σ = 8.8 meV) , OP2 (A = 1.2, μ = -19.6 meV, σ = 8.8 meV) , trion (A = 13.6, μ = -20 meV, σ = 8.8 meV) , biexciton (A = 4.0, μ = -44 meV, σ = 8.8 meV) Silane-coated quantum dots see more emission from the trion state (blue dashed line) than $PEAC_8C_{12}$-passivated quantum dots.

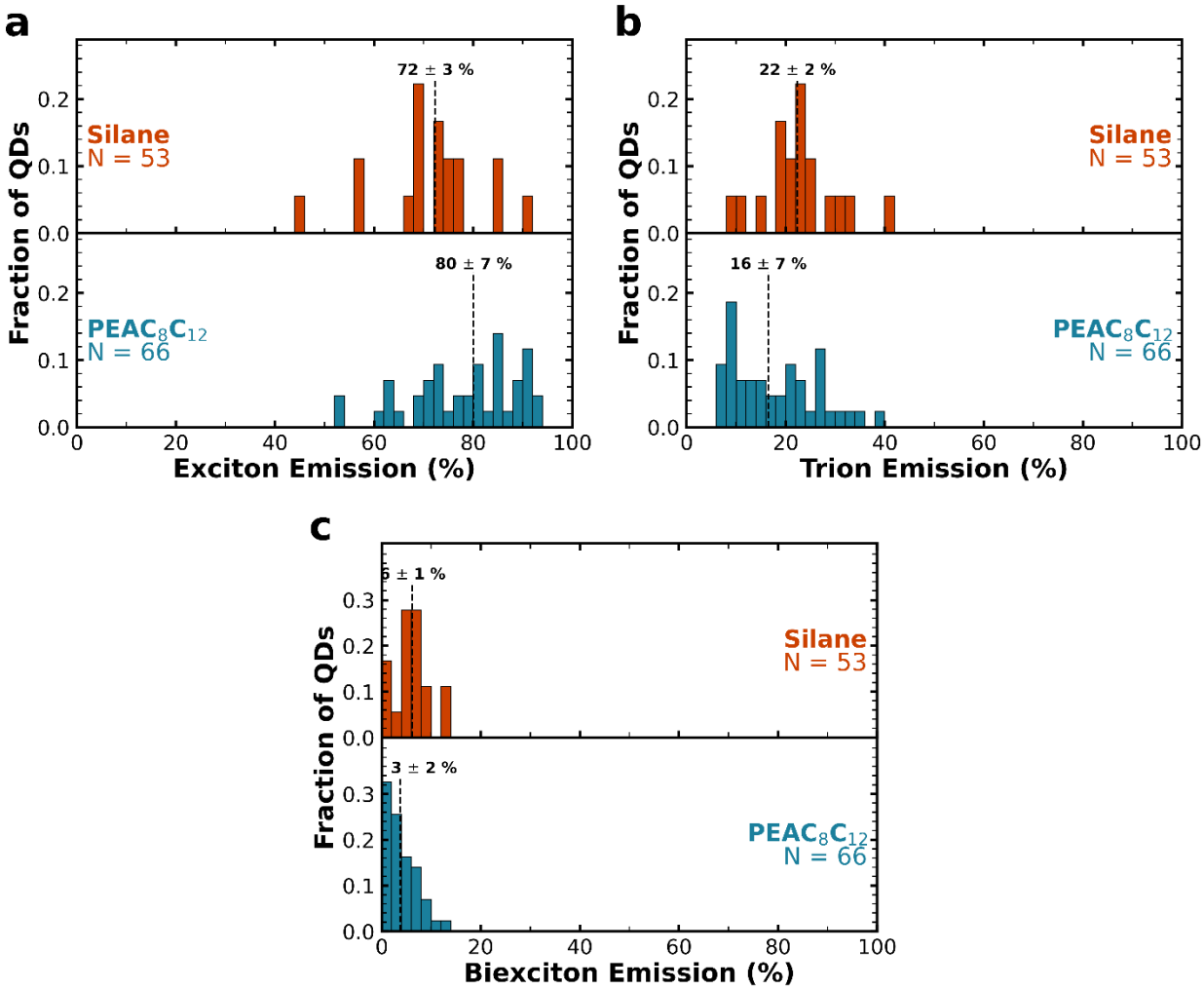

Figure S18. Photoluminescence spectra composition of single quantum dots at 4K a) exciton emission **b)** trion emission and **c)** biexciton emission

References

(1) Morad, V.; Stelmakh, A.; Svyrydenko, M.; Feld, L. G.; Boehme, S. C.; Aebli, M.; Affolter, J.; Kaul, C. J.; Schrenker, N. J.; Bals, S.; Sahin, Y.; Dirin, D. N.; Cherniukh, I.; Raino, G.; Baumketner, A.; Kovalenko, M. V. Designer Phospholipid Capping Ligands for Soft Metal Halide Nanocrystals. *Nature 2023 626:7999* **2023**, *626* (7999), 542–548. https://doi.org/10.1038/s41586-023-06932-6.

(2) Mooney, J.; Kambhampati, P. Get the Basics Right: Jacobian Conversion of Wavelength and Energy Scales for Quantitative Analysis of Emission Spectra. *Journal of Physical Chemistry Letters* **2013**, *4* (19), 3316–3318. https://doi.org/10.1021/JZ401508T.

(3) Taddei, M.; Smith, J. A.; Gallant, B. M.; Zhou, S.; Westbrook, R. J. E.; Shi, Y.; Wang, J.; Drysdale, J. N.; McCarthy, D. P.; Barlow, S.; Marder, S. R.; Snaith, H. J.; Ginger, D. S. Ethylenediamine Addition Improves Performance and Suppresses Phase Instabilities in Mixed-Halide Perovskites. *ACS Energy Lett* **2022**, *7* (12), 4265–4273. https://doi.org/10.1021/ACSENERGYLETT.2C01998.

(4) Gallagher, S.; Kline, J.; Jahanbakhshi, F.; Sadighian, J. C.; Lyons, I.; Shen, G.; Hammel, B. F.; Yazdi, S.; Dukovic, G.; Rappe, A. M.; Ginger, D. S. Ligand Equilibrium Influences Photoluminescence Blinking in CsPbBr3: A Change Point Analysis of Widefield Imaging Data. *ACS Nano* **2024**, *18* (29), 19208–19219. https://doi.org/10.1021/ACSNANO.4C04968.

(5) Palstra, I. M.; Koenderink, A. F. A Python Toolbox for Unbiased Statistical Analysis of Fluorescence Intermittency of Multilevel Emitters. *Journal of Physical Chemistry C* **2021**, *125* (22), 12050–12060. https://doi.org/10.1021/ACS.JPCC.1C01670.

(6) Li, H.; Yang, H. Statistical Learning of Discrete States in Time Series. *Journal of Physical Chemistry B* **2019**, *123* (3), 689–701. https://doi.org/10.1021/ACS.JPCB.8B10561.

(7) Tang, X.; Khurana, M.; Rossi, D.; Luo, L.; Akimov, A. V.; Son, D. H. Exciton Photoluminescence of Strongly Quantum-Confined Formamidinium Lead Bromide (FAPbBr3) Quantum Dots. *Journal of Physical Chemistry C* **2022**, *126* (43), 18366–18373. https://doi.org/10.1021/ACS.JPCC.2C05661.

(8) Yuan, G.; Gómez, D. E.; Kirkwood, N.; Boldt, K.; Mulvaney, P. Two Mechanisms Determine Quantum Dot Blinking. *ACS Nano* **2018**, *12* (4), 3397–3405. https://doi.org/10.1021/ACSNANO.7B09052.

(9) Gumbsheimer, P.; Conradt, F.; Behovits, Y.; Huber, S.; Hinz, C.; Negele, C.; Mecking, S.; Seletskiy, D. V.; Leitenstorfer, A. Enhanced Determination of Emission Fine Structure and Orientation of Individual Quantum Dots Based on Correction Algorithm for Spectral Diffusion. *J Phys D Appl Phys* **2021**, *54* (15), 155106. https://doi.org/10.1088/1361-6463/ABDA83.

(10) Cho, K.; Sato, T.; Yamada, T.; Sato, R.; Saruyama, M.; Teranishi, T.; Suzuura, H.; Kanemitsu, Y. Size Dependence of Trion and Biexciton Binding Energies in Lead Halide Perovskite Nanocrystals. *ACS Nano* **2023**, *18*, 45. https://doi.org/10.1021/ACSNANO.3C11842.

(11) Cho, K.; Yamada, T.; Tahara, H.; Tadano, T.; Suzuura, H.; Saruyama, M.; Sato, R.; Teranishi, T.; Kanemitsu, Y. Luminescence Fine Structures in Single Lead Halide Perovskite Nanocrystals: Size Dependence of the Exciton-Phonon Coupling. *Nano Lett* **2021**, *21* (17), 7206–7212. https://doi.org/10.1021/ACS.NANOLETT.1C02122.

(12) Zhu, C.; Feld, L. G.; Svyrydenko, M.; Cherniukh, I.; Dirin, D. N.; Bodnarchuk, M. I.; Wood, V.; Yazdani, N.; Boehme, S. C.; Kovalenko, M. V; Rainò, G.; Zhu, C.; Feld, L. G.; Svyrydenko, M.; Cherniukh, I.; Dirin, D. N.; Bodnarchuk, M. I.; Boehme, S. C.; Kovalenko, M. V; Rainò, G.

Quantifying the Size-Dependent Exciton-Phonon Coupling Strength in Single Lead-Halide Perovskite Quantum Dots. *Adv Opt Mater* **2024**, 2301534. https://doi.org/10.1002/ADOM.202301534.

(13) Sampat, S.; Karan, N. S.; Guo, T.; Htoon, H.; Hollingsworth, J. A.; Malko, A. V. Multistate Blinking and Scaling of Recombination Rates in Individual Silica-Coated CdSe/CdS Nanocrystals. *ACS Photonics* **2015**, *2* (10), 1505–1512. https://doi.org/10.1021/ACSPHOTONICS.5B00423.

(14) Pan, A.; He, B.; Fan, X.; Liu, Z.; Urban, J. J.; Alivisatos, A. P.; He, L.; Liu, Y. Insight into the Ligand-Mediated Synthesis of Colloidal CsPbBr3 Perovskite Nanocrystals: The Role of Organic Acid, Base, and Cesium Precursors. *ACS Nano* **2016**, *10* (8), 7943–7954. https://doi.org/10.1021/ACSNANO.6B03863.

(15) Meng, C.; Yang, D.; Wu, Y.; Zhang, X.; Zeng, H.; Li, X. Synthesis of Single CsPbBr3@SiO2 Core–Shell Particles via Surface Activation. *J Mater Chem C Mater* **2020**, *8* (48), 17403–17409. https://doi.org/10.1039/D0TC03932B.